BULLETIN OF THE POLISH ACADEMY OF SCIENCES
TECHNICAL SCIENCES, Vol. 69(1), 2021, Article number: e136218
DOI: 10.24425/bpasts.2020.136218

An active power filter based on a hybrid converter topology – Part 1

Michał GWÓŹDŹ and Łukasz CIEPLIŃSKI*

Poznan University of Technology, Faculty of Control, Robotics and Electrical Engineering, Piotrowo 3A, 60-965 Poznan, Poland

Abstract. This paper presents a concept of a shunt active power filter, which is able to provide more precise mapping of its input current drawn from a power line in a reference signal, as compared to a typical filter solution. It can be achieved by means of an interconnection of two separate power electronics converters making, as a whole, a controlled current source, which mainly determines the quality of the shunt active filter operation. One of these power devices, the "auxiliary converter", corrects the total output current, being a sum of output currents of both converters, toward the reference signal. The rated output power of the auxiliary converter is much lower than the output power of the main one, while its frequency response is extended. Thanks to both these properties and the operation of the auxiliary converter in a continuous mode, pulse modulation components in the filter input current are minimized. Benefits of the filter are paid for by a relatively small increase in the complexity and cost of the system. The proposed solution can be especially attractive for devices with higher output power, where, due to dynamic power loss in power switches, a pulse modulation carrier frequency must be lowered, leading to the limitation of the "frequency response" of the converter. The concept of such a system was called the "hybrid converter topology". In the first part of the paper, the rules of operation of the active filter based on this topology are presented. Also, the results of comparative studies of filter simulation models based on both typical, i.e. single converter, and hybrid converter topologies, are discussed.

Key words: shunt active power filter; pulse-width modulation (PWM); sigma-delta modulator; silicon carbide.

1. Introduction

The negative impact of nonlinear loads on the operation of a power grid is widely known and has been confirmed by many studies, e.g. [1–5]. Commonly used conventional solutions involving power electronics converters with diode and thyristor rectifiers, as well as functionally simplified switched-mode power supplies, draw a strongly distorted current that results in a negative impact on the power grid operation, including an increase in power loss, a reduction in grid capacity and the generation of electromagnetic disturbances. One of their direct effects is the reduction of the lifetime of both the grid itself and the loads connected to it, including those that do not have a negative impact on its operation.

In addition to the technical context, the impact of nonlinear loads should be considered in terms of purely economic and even social aspects, such as health [6]. Therefore, various types of "compensators", mainly passive [7, 8] and active filters, including shunt and serial ones [9–14], are used in electrical systems as preventive measures. The main task of these devices is the appropriate matching of the shape of the current at its input to the shape of the current drawn from the same power grid node by other loads. As a result of the compensation process understood this way, the total current, drawn from the power grid node, should have both a suitable shape and phase relation with the voltage in the power grid, depending on the compensation strategy [15–19].

Many factors affect the inaccurate mapping of a converter's output current in an input (reference) signal. The most important of these are the converter's limited frequency response, the wide-band nature of the signal sampling process and its associated aliasing phenomenon, as well as the nonlinearity of the pulse modulation process. Therefore, to meet the requirements of the accurate mapping of the converter output current in the reference signal advanced solutions of converters in hardware with respect to a multi-converter topology scenario, new converter control algorithms are necessary.

The concept of cooperation of several interconnected converters is widely used in systems related to electrical drives [20–22], converters for renewable energy sources [23] and power supply devices [24–26]. In particular, this applies to the use of two (or more) converters connected in parallel, where the output power of one of them is a fraction of the power of the second one. This concept is presented in many studies, e.g. [27–31]. A common feature of some of these solutions is that the activation of the auxiliary power electronics converter takes place only in transient states of the main converter output current.

Usually, the main role of the auxiliary converter depends on the maximisation of the dynamics of the system, i.e. the extension of its "frequency response". As a result, the total system output current is better mapped in the reference signal, compared to a single, i.e. typical, converter solution. Unfortunately,

*e-mail: Lukasz.cieplinski@put.poznan.pl

Manuscript submitted 2020-11-12, revised 2020-11-12, initially accepted for publication 2020-12-07, published in February 2021

the control algorithms of these systems, especially in relation to the auxiliary converter, are often defined in an informal way. Because of this, the potential possibilities of such systems have not been fully reached.

The subject of this work is a shunt active power filter (SAPF) with a modified topology. The power electronics voltage controlled current source (VCCS) as a fundamental block of such a filter is based on two converters connected in parallel. This architecture is called the hybrid converter topology (HCT). Therefore, the HCT concept involves the cooperative operation of two converters, but the auxiliary converter operates continuously, not only in the transient states of the system. In addition, the rules of the HCT operation are defined in a formal way. The advantage of this idea is the possibility of more accurate mapping of the SAPF input current in the reference signal, compared to the typical solution of an active filter. Moreover, unlike many other concepts of this kind, special attention is paid to the minimisation of the pulse width-modulation carrier component in the filter input current.

The following text of the work is divided into three sections. Section 1 deals with the structure and principles of operation of the SAPF based on the HCT. Section 2 presents simulation model studies for the filter. Finally, in Section 3 conclusions are presented.

2. Rules of operation of the active filter

2.1. Structure of the SAPF. Many works have been dedicated to systems for power quality monitoring and improvement. Therefore, only a brief overview of the operation of a SAPF

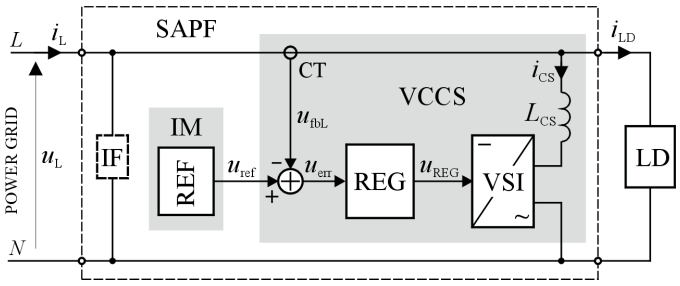

Fig. 1. Block diagram of a 1-phase SAPF

is given here. The block diagram of a typical 1-phase SAPF is shown in Fig. 1.

The SAPF consists of two main blocks, the identification module (IM) and the power electronics controlled current source, which is a power stage of the filter. The main role of the IM is to generate the reference signal (u_{ref}), which directly controls the VCCS. This task is realised in the REF block, based on the values of the voltage in the power grid node (u_L) and the load current (i_{LD}). The VCCS is composed of the following blocks: the voltage source inverter (VSI), with the inductor (L_{CS}) included at its output, the regulator (REG) of the VSI output current (i_{CS}) and the current transducer (CT), which forms the feedback signal (u_{fbL}) for the regulator. The block denoted as IF is the band-pass passive filter, which is used for minimisation in the SAPF input current of the pulse modulation carrier component, caused by operation of the converter used in the VCCS.

The power theory introduced by Fryze [15] was chosen for calculation of the reference signal; however, the concept of HCT operation, presented in this work, is not directly related to the method of determining this signal. According to the Fryze theory, the general aim of the optimisation of the power grid current (i_L) is the minimisation of its root-mean-square value. This results in the minimisation of power loss, while energy transfer from the energy source to the load (LD) occurs, among other things. Therefore, the desired resultant current, drawn from the power grid by the SAPF, is described by the following formula

$$i_L(t) = i_{LD}(t) + i_{CS}(t) = i_{ref,L}(t) = I_{ref,L}\sin(\omega_L t), \quad (1)$$

where $I_{ref,L}$ is the reference current amplitude and ω_L is the frequency of the voltage in the power grid.

Therefore, the VCCS generates the current at its input, which, when combined with the current of nonlinear load, results in a theoretically sinusoidal current, drawn from the grid. This current is also in-phase with the grid voltage. As a result, the negative impact of the nonlinear load on the power grid is eliminated, and in the real system, it is minimised.

The error signal (u_{err}), which is mainly related to the regulator, is associated with the SAPF input current based on the formula

$$u_{err} = u_{ref} - u_{fbL} = u_{ref} - r_{CT} i_L, \quad (2)$$

where r_{CT} is the transfer ratio of the CT.

The general aim of the SAPF operation is to fulfil the following equation

$$i_L = \frac{1}{r_{CT}}(u_{ref} - u_{err}) \xrightarrow{\forall\limits_{-\infty<t<\infty} u_{err} \to 0} \frac{1}{r_{CT}} u_{ref}. \quad (3)$$

By doing so, an only theoretically existing "ideal case" of the filter operation is found. However, in a real system, even a small minimisation of the error signal can be a difficult task [32–35]. Potential approaches to reduce the impact of this problem on the SAPF operation are described in the following subsection.

2.2. Basics of operation of the SAPF based on HCT. The VCCS, as a fundamental part of SAPFs, is an electrical system operating in a closed feedback loop. Many aforementioned factors, including the limited frequency response of the converter utilized in the VCCS, often cause poor mapping of the SAPF input current in the reference signal. In particular, it occurs if the value of the modulation carrier frequency is low, which is enforced by demanding the maximisation of a converter efficiency. A lower value of carrier frequency results in an increase in the magnitude of the carrier component in the filter input

current, which is a negative aspect of this system operation. Therefore, a modified arrangement of the VCCS is proposed, as shown in Fig. 2.

The HCT consists of two separate converters, forming two independent current sources. The main converter (MCN) is supported by the auxiliary converter (ACN). The MCN is a high-power device, but its frequency response is limited. In contrast, the ACN is a low-power device, but its frequency response is significantly extended, compared to the MCN. At the input of the ACN the signal limiter (LIM) is included. This one clips the ACN control signal ($u_{\mathrm{ref,A}}$) which is related directly to the error signal (u_{err}) in the control section of the main converter. The clipping levels are set at $\pm A_{\mathrm{L}}$. As a result, the LIM imposes the maximum value of the ACN output current (i_{A}) and therefore the relationship of the ACN and the MCN output power. The internal control block (ICB) is optional. This block allows for the implementation of the advanced control scenarios in the ACN.

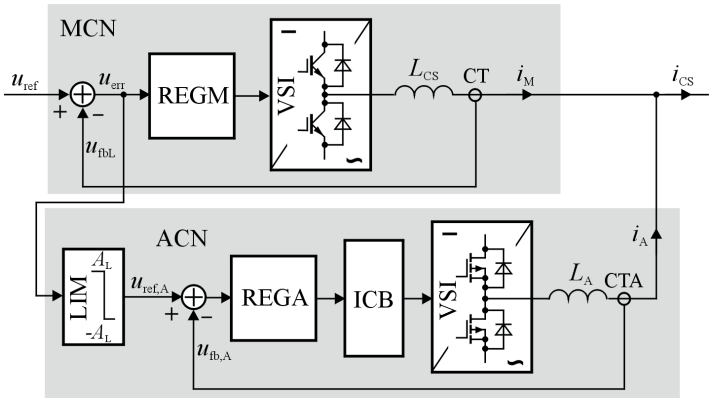

Fig. 2. Block diagram of the VCCS based on the HCT

In general, the structures of both converters can be very similar. However, the values of the main parameters of the converters are significantly different from each other. For example, to obtain an extended frequency response, the modulation carrier frequency in the ACN needs to be much higher than in the MCN. Thus, the MCN uses, for example, standard IGBT devices, while in the ACN, devices characterised by short switching times should be applied.

In a real system, both converters are powered using common DC rails. Thus, the operating voltage of the power electronics switches utilised are similar, while these devices differ in the rated output current and dynamic parameters. For a proper SAPF operation it is important that a specific phenomenon, which usually occurs in multi-channel converters, does not occur in the case of the HCT-based system. This phenomenon depends on the possibility of an unbalanced current flow in particular converter channels [24, 26]. In the case of the presented solution, due to both current paths in the HCT being controlled independently and considering the typical conditions of a SAPF operation, such an undesirable interaction between the converters is negligible.

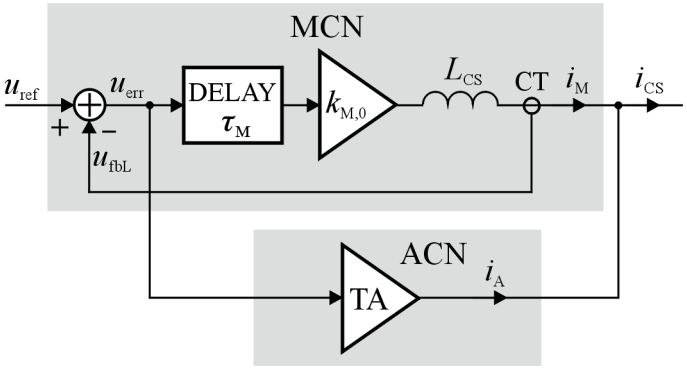

Fig. 3. Block diagram of the VCCS-HCT linear model

To present the general principles of the VCCS-HCT action, its basic linear model was considered, as shown in Fig. 3.

In this model the ACN is equipped with a transconductance amplifier (TA). Furthermore, the DELAY block is included in the model. This introduces a time delay (τ_{M}), reflecting delays occurring in a real system, resulting from the signal sampling period that is associated with the sample-and-hold amplifier operation (although these amplifiers are not shown in the figures), the time needed for signal processing, and the period of the pulse modulation carrier signal.

With respect to the HCT, the most general formula of the VCCS operation is modified to

$$i_{\mathrm{CS}} = i_{\mathrm{M}} + i_{\mathrm{A}}, \tag{4}$$

and, in the relationship to the linear model of the VCCS, it is as follows

$$i_{\mathrm{CS}} = i_{\mathrm{M}} + u_{\mathrm{err}} * g_{\mathrm{TA}} = i_{\mathrm{M}} + (u_{\mathrm{ref}} - r_{\mathrm{CT}} i_{\mathrm{M}}) * g_{\mathrm{TA}}, \tag{5}$$

where g_{TA} is the pulse response of the TA and "*" is the symbol of the convolution.

Equation (5) is true under the condition that the instantaneous value of the error signal is in the range of $\langle -A_{\mathrm{L}}, A_{\mathrm{L}} \rangle$. Then, assuming that the transfer function of the transconductance amplifier has the zero-order form, i.e. $g_{\mathrm{TA}}(t) = g_{\mathrm{TA,0}}\delta(t)$, the general equation describing the linear model operation now takes the form of Eq. (6). This equation indicates that the VCCS output current can match the reference signal regardless of the degree of mapping in this signal of the main converter output current (i_{MCN}). However, it is possible under the aforementioned condition that the magnitude of the auxiliary converter control signal is not clipped in the LIM block.

$$\begin{aligned} i_{\mathrm{CS}} &= i_{\mathrm{M}} + u_{\mathrm{ref}} * g_{\mathrm{TA,0}}\delta - r_{\mathrm{CT}} i_{\mathrm{M}} * g_{\mathrm{TA,0}}\delta = \\ &= g_{\mathrm{TA,0}} u_{\mathrm{ref}} + (1 - g_{\mathrm{TA,0}} r_{\mathrm{CT}}) i_{\mathrm{M}}\big|_{g_{\mathrm{TA,0}} r_{\mathrm{CT}} = 1} = \\ &= g_{\mathrm{TA,0}} u_{\mathrm{ref}} \wedge u_{\mathrm{err}} \subset \langle -A_{\mathrm{L}}, A_{\mathrm{L}} \rangle \end{aligned} \tag{6}$$

In turn, the extended linear model of the VCCS-HCT is shown in Fig. 4. This model was used for system stability analysis, based on the Nyquist criterion.

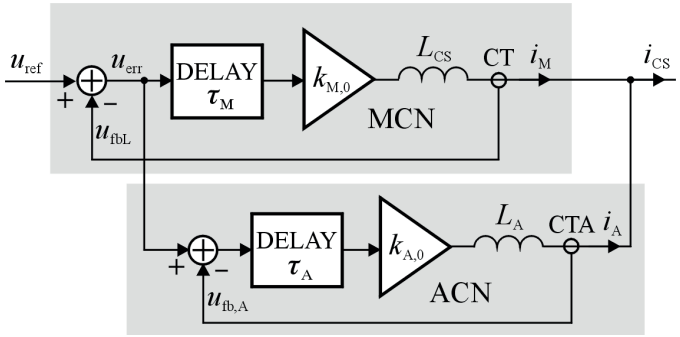

Fig. 4. Block diagram of the VCCS extended linear model based on the HCT concept

The model of the VCCS is both SISO and LTI type [32, 34] and can be described in the frequency domain by

$$I_{CS}(j\omega) = U_{ref}(j\omega)\frac{1}{r_{CT}}\frac{e^{-j\omega\tau_M}}{j\omega\frac{L_{CS}+L_L}{k_{M,0}r_{CT1}}+e^{-j\omega\tau_M}} + \\ + U_{err}(j\omega)\frac{1}{r_{CTA}}\frac{e^{-j\omega\tau_A}}{j\omega\frac{L_A+L_L}{k_{A,0}r_{CTA}}+e^{-j\omega\tau_A}} \wedge \\ \wedge\, u_{err} \subset \langle -A_L, A_L\rangle \wedge R_L = 0, \tag{7}$$

where $k_{M,0}$ is the gain of the current regulator in the MCN; $k_{A,0}$ is the gain of the regulator in the CAN; τ_M is the time delay introduced in the MCN; τ_A is the time delay introduced in the CAN; L_{CS} is the inductance of the reactor in the MCN; L_A is the inductance of the reactor in the CAN; r_{CTA} is the transfer factor of the CTA; L_L is the grid inductance; and R_L is the grid resistance.

The maximum gains of the regulators (REGM, REGA) are limited due to needs of preventing the system stability.

Assuming the regulators are P (proportional) type, the values of these gains are given by the following equations [33]

$$k_{M,0,max} < 2\frac{L_{CS}+L_L}{r_{CT}\tau_M}, \tag{8}$$

$$k_{A,0,max} < 2\frac{L_A+L_L}{r_{CT}\tau_A}, \tag{9}$$

where $r_{CTA} = r_{CT}$.

These equations do not consider the reactors and the grid resistance. However, for typical values of these quantities, their influence on the permissible gain value of the regulator is negligible, while the complexity of the equations clearly increases.

Considering Eq. (8) and Eq. (9), Eq. (7) now takes the form of Eq. (10). The first part of this equation expresses the best, for mapping the VCCS's output current in the reference signal, conditions of this system operation, while second one presents a boundary condition $(p \to \infty)$ of the system action. In other words, for an effective SAPF operation the following should hold: $f_{c,A} \gg f_{c,M}$ and $f_A \ll f_M$, where $f_{c,M}$ and $f_{c,A}$ are pulse modulation carrier frequencies in the MCN and the ACN, respectively.

By fulfilling Eq. (10) the VCCS-HCT frequency response is now approximately p-times extended, compared to the MCN one. Therefore, the dominant effect on the quality of the VCCS output current, in the sense of minimising the error signal, is to set both $f_{c,A}$ and A_L at the highest levels as possible. However, increasing $f_{c,A}$ results directly in the lowering of the converter efficiency, while a high value of A_L enforces, automatically, a higher value of the rated output power of the ACN.

There are a few possible topologies of the ACN. For the subsequent studies, the converter based on the continuous-time sigma-delta modulator (SDM) in the control block was selected. The properties, as well as the rules of operation of the converter, based on such a modulator, are given in the next subsection.

2.3. Basics of operation of the continuous-time SDM. The self-exciting continuous-time SDM [36–39], with a dynamic hysteresis comparator (DHC) [40], was proposed to control the power stage of the ACN. The basic premise of the ACN is to obtain the precise mapping of its output current to the reference (input) signal, which is in-line with the SDM-DHC properties. Formally, the SDM-DHC is the ICB of the ACN.

From the point of view of the SDM-DHC operation its output signal is both PWM- and PDM-modulated [36, 40]. Theoretically, due to the analogue nature of the SDM-DHC, its resolution tends toward infinity. In addition, both the gain value and pass-band of this system reach considerable values. As a result of these properties, the value of distortions of the ACN output current is lower compared to typical, i.e. PWM-based solutions [9, 10, 40]. Moreover, in contrast to SDMs based on a static hysteresis comparator, equipped with the R-R network, in the case of the SDM-DHC the minimal width of its output pulses is limited to a certain pre-set value.

$$I_{CS}(j\omega) = \frac{U_{ref}(j\omega)}{r_{CT}}\frac{e^{-j\omega\tau_M}}{j\omega\frac{T_M}{2}+e^{-j\omega\tau_M}} + \frac{U_{err}(j\omega)}{r_{CTA}}\frac{e^{-j\omega\frac{\tau_M}{p}}}{j\omega\frac{T_M}{2p}+e^{-j\omega\frac{\tau_M}{p}}} = \frac{1}{r_{CT}}\left[\frac{U_{ref}(j\omega)}{1+j\omega\frac{T_M}{2}e^{j\omega\tau_M}} + \frac{U_{err}(j\omega)}{1+j\omega\frac{T_M}{2p}e^{j\omega\frac{\tau_M}{p}}}\right] \xrightarrow{p\to\infty} \\ \xrightarrow{p\to\infty} \frac{1}{r_{CT}}\left[U_{ref}(j\omega)\frac{1}{1+j\omega\frac{T_M}{2}e^{j\omega\tau_M}} + U_{err}(j\omega)\right] \wedge\; u_{err} \subset \langle -A_L, A_L\rangle \wedge\; p = \frac{\tau_M}{\tau_A} \tag{10}$$

This value depends on the time constant of the DHC [40]. Therefore, the DHC is insensitive to high-frequency pulses, e.g. noise in its input signal. Consequently, such a device is more resistant to electromagnetic disturbances, compared to a system based on a comparator with a static hysteresis. The structure of the SDM-DHC, as the converter control unit is simple, has no complex digital components. A modulator of this kind can be easily implemented in electronics or power electronic devices, where a high quality of output current (or voltage) is necessary [41–45]. However, most examples of such converters are class-D audio amplifiers [46–48].

The details of operating of the SDM based on the DHC are presented in the previous work [40]. Therefore, only a brief description of this system topology and its basic properties is given here in relation to the "signal non-inverting" version of the DHC, as shown in Fig. 5.

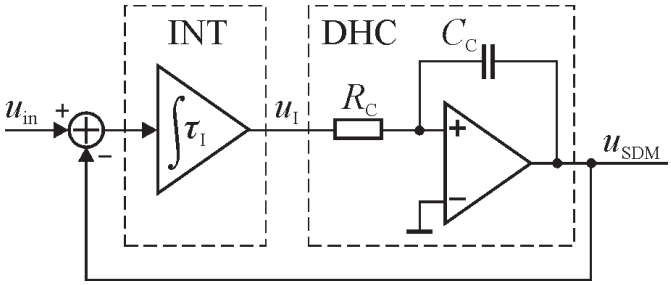

Fig. 5. Block diagram of the SDM with DHC in a "signal non-inverting" version

Basically, the SDM contains two main blocks, an integrator (INT) and a dynamic hysteresis comparator (DHC), which are characterised by the τ_I and τ_C time constants, respectively. These blocks operate in a closed feedback loop. At the output of the DHC a power stage is typically included, but this block is not shown in Fig. 5.

The SDMs are difficult to analyse in the time domain because of their apparent randomness of the output bit-stream. Formally, the system is both nonlinear and time variant [36–39]. Thus, a strict analytical description of the SDM-DHC operation is very difficult or even impossible. Usually, simplified models of an SDM in the frequency domain are in use. These models are also utilised for system stability analysis [35–39]. Most of the equations and relationships included in this work were obtained based on heuristic methods [49, 50] and then confirmed by both simulation and experimental model studies. Thus, the basic dependencies in the SDM are as follows:

- Period of the SDM output signal

$$T_{SDM} = 5\tau_C\big|_{\tau_I = 3\tau_C,\, m=0}, \tag{11}$$

where $\tau_C = R_C C_C$ and m is the pulse modulation index, which is defined as

$$m = k_{SDM,0}\frac{\overline{u_{in}}}{U_{SDM}} \wedge \left|u_{in}\right| \le U_{SDM} \wedge m \in \langle -1, 1\rangle, \tag{12}$$

where u_{in} is the SDM input signal; U_{SDM} is the magnitude of the DHC output signal; and $k_{SDM,0}$ is the SDM's gain for DC.

- Relationship of the integrator and comparator time constants, which protects the output of the integrator against entering a saturation (signal clipping) state

$$\tau_I \ge 3\tau_C. \tag{13}$$

- Minimal width of the DHC input signal being passed through itself, assuming that the shape of the DHC input signal is rectangular and its magnitude is equal to the magnitude of the DHC output signal

$$T_{C,min} = \left|\ln\frac{1}{3}\right|\tau_C \cong 1.1\tau_C. \tag{14}$$

For maximisation of the converter frequency response, the value of τ_I should be as small as possible. However, Eq. (13) must be respected. Therefore, the SDM generates a PWM similar signal with a "carrier period", the value of which depends on both the DHC and the integrator time constants. The value of the carrier period varies with the input signal magnitude of the SDM, i.e. the modulation index. This dependency is presented in Fig. 6. Thus, the frequency of the SDM output bit-stream is a spread spectrum in nature. However, spread spectrum techniques are applied to distribute the electromagnetic emissions over a wider frequency range [51, 52].

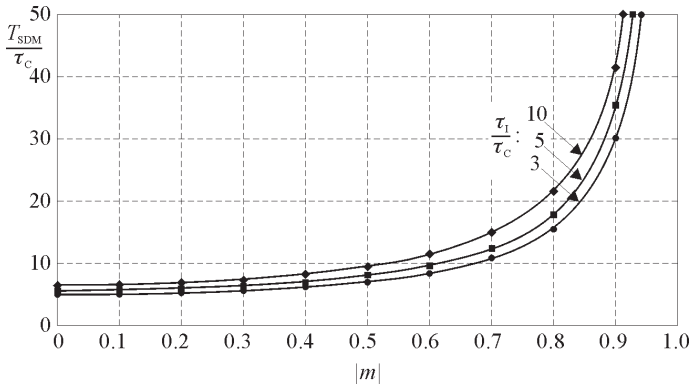

Fig. 6. Relative value of the SDM "carrier period" versus modulation index, while the relationship of the integrator and DHC time constants varies

In the case of $m = 0$, the SDM generates a rectangular signal with a 50% value of the duty factor. If $|m| > 0.9$, the carrier frequency decreases rapidly. Therefore, with further consideration, it was assumed that the SDM operates in the range of $|m| \le 0.9$.

An advantage in decreasing the value of the pulse modulation carrier frequency with the increase of the modulation index is the increase in the efficiency of the converter. However, it is also associated with increasing the magnitude of ripples in the converter output current, which lowers its quality.

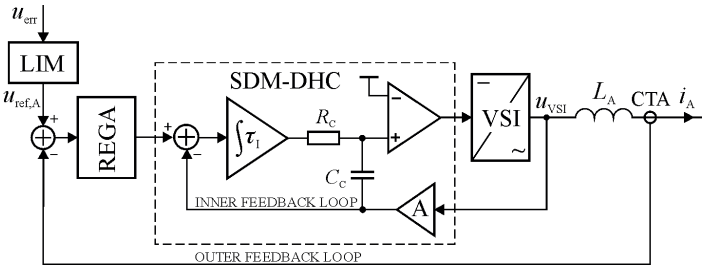

Fig. 7. Block diagram of the ACN based on the SDM-DHC

Figure 7 shows the block diagram of the ACN based on the SDM-DHC. Its general topology is consistent with Fig. 2 and, in terms of the method of control of the VSI, it is also in agreement with Fig. 5.

The ACN uses two feedback loops, the SDM's inner loop, associated with the voltage at the output of the VSI, and the outer one, associated with the ACN output current. The block denoted as A is the attenuator of the VSI output voltage. The attenuator is necessary in this system because the value of the feedback signal magnitude must be consistent with the magnitudes of the other modulator's internal signals.

3. Studies of the SAPF simulation models

To check the theoretical assumptions, comparative studies on the simulation models of the SAPF, based on both the HCT and typical topology, i.e. based on a single converter (SCT), with the use of the ORCAD/SPICE environment, were conducted. These tests were mainly devoted to determining the ability of the VCCS-HCT to map its output current in the reference signal, in terms of cooperation with a "real" power grid, which is characterised by, among other factors, a non-zero internal impedance.

The block scheme of the SAPF simulation model, based on the HCT, is shown in Fig. 8. The structure of a single phase of the model is shown for better clarity.

Considering a possible practical arrangement of the VCCS in the future, the models of IGBT modules were used in the main converter. A good choice seems the seventh generation NX-type [53], which represents a low power loss family of power devices, manufactured by Mitsubishi Electric. In this case, the 3-branch, 1200 V/150 A, CM150-TX24T device was selected. In the auxiliary converter the model of the recent device, developed by Infineon Technologies, the 3-branch, 1200 V/25 A, SiC MOSFET module type FS45MR12W1M1_B11 [54], was used. The operating conditions of these modules were selected based on the values recommended by their manufacturers, including the permissible power loss, related to voltage, current, and switching frequency.

Ready-to-use models of power electronics switches that are available in the SPICE environment were modified toward real devices. However, only basic, static, and dynamic, parameters of these power modules were considered. Additionally, the correctness of the simulation models, in terms of the power loss, was checked by comparing the simulation results, obtained in SPICE, with results achieved with the dedicated simulation software, available on the websites of both manufacturers of the power devices.

In the control block of the converters three types of current regulator were tested: P, PI, and the combination of these. However, the presented simulation tests results assume the P version of the regulator, which is not typical in such systems, but the HCT properties are, in this case, visibly better compared to other types of regulators.

The quality of the SAPF operation was evaluated based on values of the following quantities:

- *TTHD* of the SAPF input current, which is related to the *TTHD* of the load current.
- Control error (ε_1), related to the amplitude of the basic harmonics of the SAPF input current (I_{L1}) and the amplitude of the reference signal

$$\varepsilon_1 = \left| 1 - \frac{r_{CT} I_{L1}}{U_{ref}} \right| 100\% , \tag{15}$$

where U_{ref} is the amplitude of reference signal.

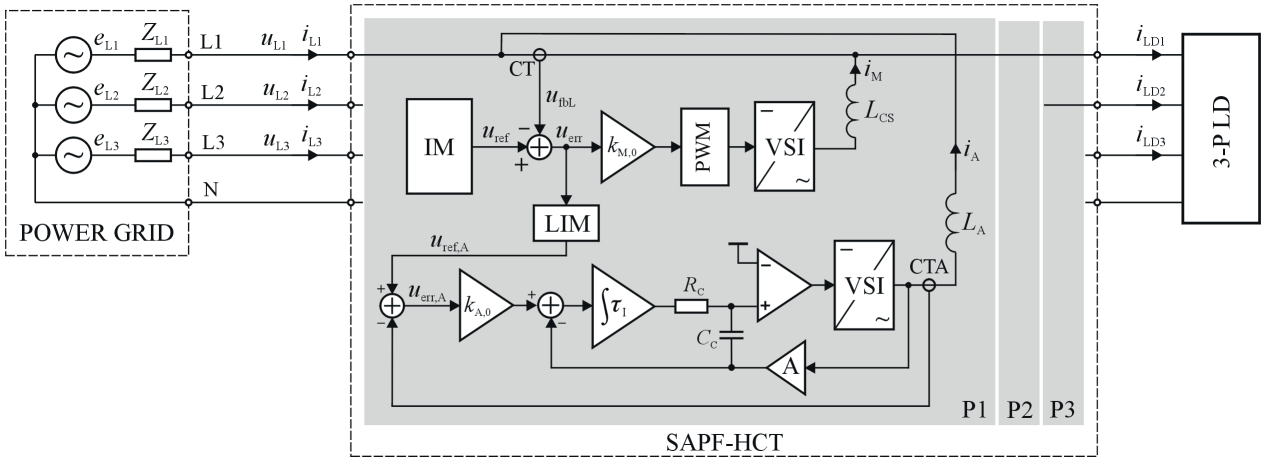

Fig. 8. Block diagram of the SAPF-HCT simulation model

- Relationship of the amplitude of the PWM carrier component in the SAPF input current ($I_{c,L1}$) and the amplitude of the reference signal (α)

$$\alpha = \frac{r_{CT} I_{c,L1}}{U_{ref}} 100\% . \tag{16}$$

The basic electrical parameters of the power grid and SAPF models are as follows:

- Power grid type: 4-wire, 230 V/50 Hz
- Power grid impedance: 0.06 Ω
- Filter's rated output power: 32 kVA
- PWM carrier frequency in the MCN: $f_{c,M} = 5$ kHz
- "Nominal" value of the pulse modulation carrier frequency in the ACN: $f_{c,A} = 200$ kHz ($m = 0$)
- Reactor's inductance: $L_{CS} = 2.0$ mH, $L_A = 0.2$ mH
- Maximum magnitude of the converters output currents: 75 A for the MCN and 15 A for the ACN

The rated output power of the ACN was equal to approximately 15% of the rated output power of the MCN. This value was chosen, as a result of extensive studies, as a good compromise between the expected effectiveness of the SAPF operation and economic aspects of a system design.

A few different types of SAPF loads, represented by 3-P LD block (Fig. 8), were considered during the studies. These included both symmetrical and asymmetrical types, 3- and 4-wire ones. However, three of these, which are characteristic for typical conditions of the real SAPF operation [9, 10], are presented in the following section. These comprehensively present the most important features of the presented system:

- Load No. 1: 3-phase thyristor voltage regulator loaded by resistor; the fire angle was set at 90°.
- Load No. 2: 6-pulse diode rectifier, loaded by a resistor, with a large capacitor (330 μF) in the DC link; for limitation of magnitudes of current pulses in the rectifier input current, caused by the capacitor, an inductor (100 μH) at the output of rectifier was included.
- Load No. 3: resistor and a large inductor (30 mH) were connected in a series.

In the case of load No. 1, the value of the slew rate of the current was extremely high, which enforced particularly high requirements regarding the effectiveness of the filter operation, in the sense of its dynamics. In turn, in the case of load No. 3, theoretically, only a reactive power was generated, allowing for better observation of the system's specific features.

The presented tests were conducted with the further assumption made that the value of the VCCS output current magnitude is close to the maximum one. The selected waveforms in the SAPF simulation model are shown in Figs. 9–11. These wave-

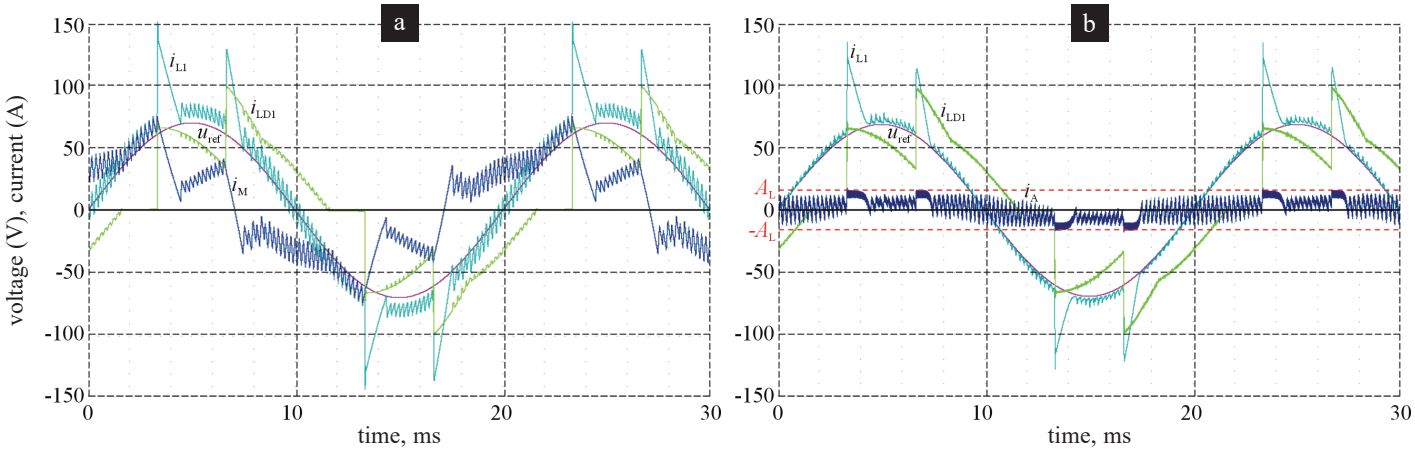

Fig. 9. Selected waveforms in the simulation model of the SAPF for load No. 1: a) SCT; b) HCT

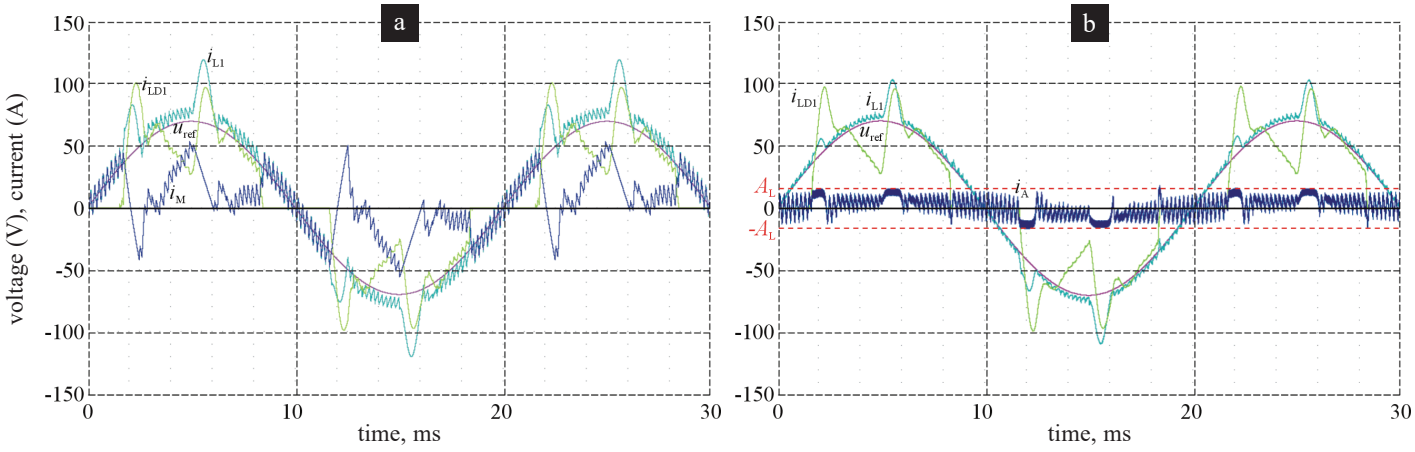

Fig. 10. Selected waveforms in the simulation model of the SAPF for load No. 2: a) SCT; b) HCT

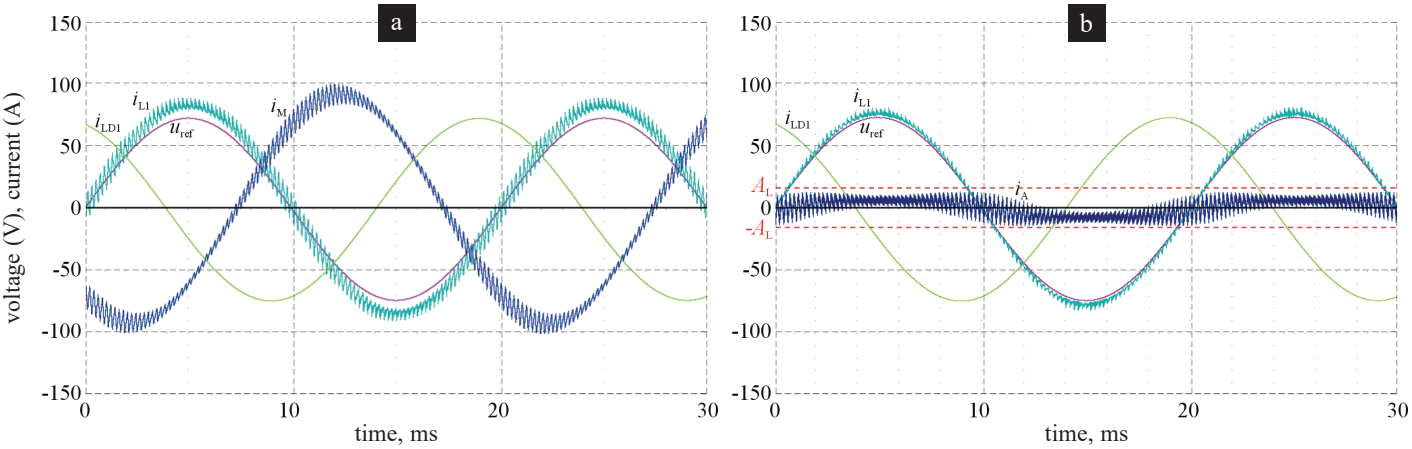

Fig. 11. Selected waveforms in the simulation model of the SAPF for load No. 3: a) SCT; b) HCT

forms are the reference signal for the filter, the load current, the output current of the VCCS, and the input current of the SAPF. In the case of the HCT also the error signal clipping levels ($\pm A_L$) and the ACN output current are shown. Waveforms in only a single phase of the model are shown for better visibility.

In Table 1 selected parameters of the load current and the SAPF input current are presented, for the aforementioned three kinds of load and both types of filter. All values are related to the phase No. 1 (L1) of voltage in the grid.

Table 1
Results of SAPF simulation model studies

No. of load	*TTHD* of load current [%]	*TTHD* of SAPF input current [%]		ε_1 [%]		α [%]	
		SCT	HCT	SCT	HCT	SCT	HCT
1	32.0	22.0	20.3	21.8	14.6	7.2	1.2
2	45.4	18.2	15.2	16.7	10.3	6.1	1.1
3	0	2.4	0.4	12.3	4.0	7.1	1.4

Depending on the type of load, the following relationships take place:

- *TTHD* of the SAPF input current is reduced 1.1–6.0 times for the HCT, compared to the SCT.
- ε_1 for the HCT is reduced 1.5–3.1 times, compared to the filter based on the SCT.
- α, in the case of the SAPF-HCT, is reduced 5.6 times, on average, compared to the SAPF-SCT.

These results clearly show a more efficient operation of the active filter based on the HCT, compared to the SAPF-SCT. This is particularly seen in relation to the degree of reduction in the filter input current of the PWM components, generated in the MCN.

In turn, in Fig. 12, the spectrum of the filter input current for both filter topologies is shown, for load No 3.

In the case of the VCCS-HCT (red plot), the spectrum of the filter input current is visible spread and the magnitudes of the PWM components are significantly lowered, compared to

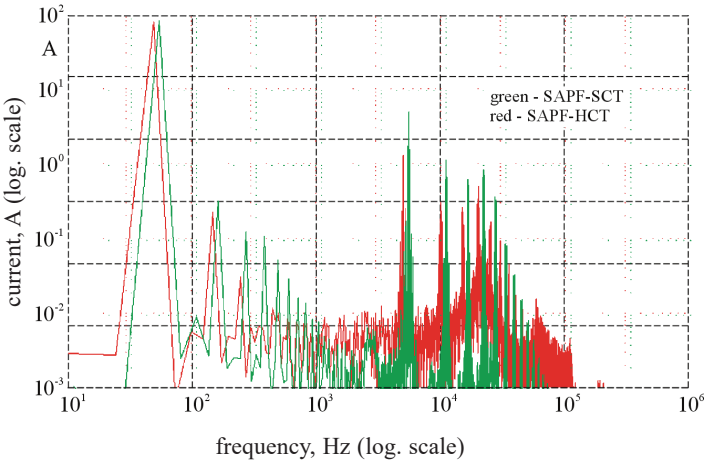

Fig. 12. Spectrum of the SAPF-SCT and SAPF-HCT input currents

VCCS-SCT; the dominant components of the pulse modulation, coming from the ACN, are in the range of 10–100 kHz.

4. Conclusions

In this work, the concept of a shunt active power filter with the modified structure of the power stage is presented. The power electronics controlled current source, as a basic part of such a filter, uses the hybrid converter topology, consisting of two converters connected in parallel and differing in the rated output power and frequency response. The output power of the main converter is several times higher than the power of the auxiliary one, while the frequency response of the auxiliary converter is significantly extended.

In the discussion in this work, the rated output power of the auxiliary converter was equal to 15% of the output power of the main converter, while its frequency response is on average extended up to 10 times. Benefitting from the cooperation of both converters in a continuous manner, this topology facilitates better filter input current mapping in the reference signal, compared to a typical converter solution. Moreover, it is

possible even in the case of a very simplified topology of the current regulator. Considering commonly used criteria for the evaluation of the quality of active filter input current, the HCT allows for improving this current 1.1–6.0 times, compared to the typical SAPF solution, including visible minimisation of the pulse-width modulation components.

What is important, the rules of the SAPF-HCT operation are not assigned to a specific power theory and this operation is inherently resistant to possible asymmetries of both the power grid and load. These benefits are paid for by a relatively small increase in the system complexity and the estimated system production cost.

In addition to the SAPF discussed in this study, the other expected areas for the application of the proposed HCT solution are energy flow controllers in power lines, electric drives, and converters for renewable energy sources. However, in these cases, some modifications of the converter topology could be necessary.

References

[1] B. Kroposki, C. Pink, R. DeBlasio, H. Thomas, M. Simões, and P. Sen, "Benefits of Power Electronic Interfaces for Distributed Energy Systems", *IEEE Trans. Energy Convers.* 25, 901–908 (2010).

[2] M. Pasko, D. Buła, K. Dębowski, D. Grabowski, and M. Maciążek, "Selected methods for improving operating conditions of three-phase systems working in the presence of current and voltage deformation — Part I", *Arch. .Electr. Eng.* 67, 591–602 (2018).

[3] A. Benchabira and M. Khiat, "A hybrid method for the optimal reactive power dispatch and the control of voltages in an electrical energy network", *Arch. Electr. Eng.* 68, 535–551 (2019).

[4] A. Nami, J.L. Rodríguez Amenedo, S. Arnaltes Gómez, and M.Á. Cardiel Álvarez, "Active power filtering embedded in the frequency control of an offshore wind farm connected to a diode-rectifier-based HVDC link", *Energies* 11, 2718 (2018).

[5] A.J. Christe, S. Negrashov, and P.M. Johnson, "Design, implementation, and evaluation of open power quality", *Energies* 13, 4032 (2020).

[6] B. Lewczuk, G. Redlarski, A. Zak, N. Ziółkowska, B. Przybylska-Gornowicz, and M. Krawczuk, "Influence of Electric, Magnetic, and Electromagnetic Fields on the Circadian System: Current Stage of Knowledge", in *BioMed Research International 2014*, 2014, pp. 1–13.

[7] M. Siwczyński and M. Jaraczewski, "Reactive compensator synthesis in time-domain", *Bull. Pol. Ac.: Tech*. 60(1), 119–124 (2012).

[8] Y. Chen, Z. Huang, Z. Duan, P. Fu, G. Zhou, and L. Luo, "A four-winding inductive filtering transformer to enhance power quality in a high-voltage distribution network supplying nonlinear loads", *Energies* 12, 2021 (2019).

[9] Y. Rozanov, S. Ryvkin, E. Chaplygin, and P. Voronin, *Fundamentals of power electronics: operating principles, design, formulas, and applications*, CRC Press, 2015.

[10] M. Rashid, *Power Electronics Handbook*, Elsevier Ltd.: Oxford, 2018.

[11] K. Shyu, M. Yang, Y. Chen, and Y. Lin, "Model Reference Adaptive Control Design for a Shunt Active-Power-Filter System", *IEEE Trans. Ind. Electron.*55, 97–106 (2008).

[12] A. Kouzou, M. Mahmoudi, and M. Boucherit, "Evaluation of the Shunt Active Power Filter apparent power ratio using particle swarm optimization", *Arch. Control Sci.* 20, 47–76 (2010).

[13] K. Mikołajuk and A. Toboła, "Average time–varying models of active power filters", *Prz. Elektrotechniczny* 95, 53–55 (2010).

[14] M. Gwóźdź, "Power electronics active shunt filter with controlled dynamics", *Compel-Int. J. Comp. Math. Electr. Electron. Eng.* 32, 1337–1344 (2013).

[15] S. Fryze, "Active, reactive, and apparent power in circuits with nonsinusoidal voltage and current", *Prz. Elektrotechniczny* 13, 193–203 (1931).

[16] M. Artemenko, L. Batrak, and S. Polishchuk, "New definition formulas for apparent power and active current of three-phase power system", *Prz. Elektrotechniczny* 95, 81–85 (2019).

[17] H. Akagi, "Modern active filters and traditional passive filters", *Bull. Pol. Ac.: Tech*. 54(3), 255–269 (2006).

[18] H. Akagi, E. Watanabe, and M. Aredes, *Instantaneous power theory and applications to power conditioning*, IEEE Press, Hoboken: Piscataway, 2017.

[19] L. Czarnecki, "Effect of Supply Voltage Harmonics on IRP-Based Switching Compensator Control", *IEEE Trans. Power Electron.* 24, 483–488 (2009).

[20] J. Vásárhelyi, M. Imecs, C. Szabó, I. Incze, and Á. Tihamér, "Managing transients generated by the reconfiguration process at the tandem inverter fed induction motor", *Proceedings of IEEE 7th International Conference on Intelligent Engineering Systems*, 2003, pp. 388–393.

[21] K. Kaneko, J. Mitsuta, K. Matsuse, K. Sasagawa, Y. Abe, and L. Huang, "Analysis of dynamic variation on a combined control strategy for a five-level double converter", *Proceedings of Power Electronics Specialists Conference PESC '05*, 2005, pp. 885–891.

[22] M. Imecs, A. Trzynadlowski, I. Incze, and C. Szabo, "Vector Control Schemes for Tandem-Converter Fed Induction Motor Drives", *IEEE Trans. Power Electron.* 20, 493–501 (2005).

[23] T. Morizane and N. Kimura, "Circulating current control of double converter system for wind power generation", *Proceedings of the 14th European Conference on Power Electronics and Applications (EPE 2011)*, 2011.

[24] A. Tomaszuk and A. Krupa, "High efficiency high step-up DC/DC converters – a review", *Bull. Pol. Ac.: Tech*. 59(4), 475–483 (2011).

[25] M. Gwóźdź, Ł. Ciepliński, and M. Krystkowiak, "Power supply with parallel reactive and distortion power compensation and tunable inductive filter — Part 1", *Bull. Pol. Ac.: Tech*. 68(3), 401–408 (2020).

[26] X. Rui, L. Jing, L. Fuzhong, and W. Zhi, "The application on active noise cancellation — Research on the series-parallel compensated UPS converter", *International Symposium on Electromagnetic Compatibility EMC 2007*, China, 2007, pp.138–141.

[27] L. Asiminoaei, E. Aeloiza, P. Enjeti, and F. Blaabjerg, "Shunt Active-Power-Filter Topology Based on Parallel Interleaved Inverters", *IEEE Trans. Ind. Electron.* 55, 1175–1189 (2008).

[28] G. Eirea and S. Sanders, "Phase Current Unbalance Estimation in Multiphase Buck Converters", *IEEE Trans. Power Electron.* 23, 137–143 (2008).

[29] M. Hirakawa, M. Nagano, Y. Watanabe, K. Ando, S. Nakatomi, S. Hashino, and T. Shimizu, "High power density interleaved dc/dc converter using a 3-phase integrated close-coupled inductor set aimed for electric vehicles", *Proceedings of Energy Conversion Congress and Exposition (ECCE) 2010*, 2010, pp. 2451–2457.

[30] J. Iwaszkiewicz, P. Bogusławski, A. Krahel, and E. Łowiec, "Three-phase voltage outages compensator with cascaded multilevel converter", *Arch. Electr. Eng.* 61, 325–336 (2012).

[31] J. Wu, H. Jou, P. Huang, and I. Chiu, "Current balancing control for an interleaved boost power converter", *Int. J. .Electron.* 106, 1567–1582 (2019).

[32] M. Schetzen, *Linear time-invariant systems*, Wiley-IEEE Press, 2003.

[33] M. Gwóźdź, "Stability of discrete time systems on base of generalized sampling expansion", *Elektryka*, Silesian University of Technology 57, 29–40 (2011).

[34] J. Doyle, B. Francis, and A. Tannenbaum, *Feedback Control Theory*, Dover Publications, 2013.

[35] Y. Hasegawa, *Control Problems of Discrete-Time Dynamical Systems*, Springer, 2015.

[36] W. Kester, *The Data Conversion Handbook, Analog Devices Inc*, Newnes, 2005.

[37] J. de la Rosa, "Sigma-Delta Modulators: Tutorial Overview, Design Guide, and State-of-the-Art Survey", *IEEE Trans. Circuits Syst. I-Regul. Pap.* 58, 1–21 (2011).

[38] A. Jain, M. Venkatesan, and S. Pavan, "Analysis and Design of a High Speed Continuous-time Delta Sigma Modulator Using the Assisted Opamp Technique", *IEEE J. Solid-State Circuit.* 47, 1615–1625 (2012).

[39] B. Razavi, "The Delta-Sigma Modulator [A Circuit for All Seasons]", *IEEE Solid-State Circuit. Mag.* 8, 10–15 (2016).

[40] M. Gwozdz and D. Matecki, "Power electronics inverter with a modified sigma-delta modulator and an output stage based on GaN E-HEMTs", in *Advanced Control of Electrical Drives and Power Electronic Converters*, pp. 327–338 Springer, London, 2017.

[41] J. Chen, Y. Hwang, C. Jheng, Y. Ku, and C. Yu, "A Low-Electromagnetic-Interference Buck Converter with Continuous-Time Delta-Sigma-Modulation and Burst-Mode Techniques", *IEEE Trans. Ind. Electron.* 65, 6860–6869 (2018).

[42] D. Gerber, C. Le, M. Kline, P. Kinget, and S. Sanders, "An Integrated Multilevel Converter with Sigma–Delta Control for LED Lighting", *IEEE Trans. Power Electron.* 34, 3030–3040 (2019).

[43] B. Jacob and M. Baiju, "Space-Vector-Quantized Dithered Sigma–Delta Modulator for Reducing the Harmonic Noise in Multilevel Converters", *IEEE Trans. Ind. Electron.* 62, 2064–2072 (2015).

[44] C. Chang, F. Wu, and Y. Chen, "Modularized Bidirectional Grid-Connected Inverter with Constant-Frequency Asynchronous Sigma-Delta Modulation", *IEEE Trans. Ind. Electron.* 59, 4088–4100 (2012).

[45] B. Wilamowski and J. Irwin, Fundamentals of Industrial Electronics, CRC Press: London, United Kingdom, 2017.

[46] Y. Kang, T. Ge, H. He, and J. Chang, "A review of audio class D amplifiers", *2016 International Symposium on Integrated Circuits (ISIC)*, Singapore, 12–14 (2016).

[47] X. Jiang, "Fundamentals of Audio Class D Amplifier Design: A Review of Schemes and Architectures", *IEEE Solid-State Circuits Magazine* 9, 14–25 (2017).

[48] G. Scott, "Design Considerations for Class-D Audio Power Amplifiers", in Application Report (SLOA242A), Texas Instruments, 2019.

[49] A. Chatterjee, H. Nobahari, and P. Siarry, *Advances in Heuristic Signal Processing and Applications*, Springer: Berlin, Heidelberg, 2013.

[50] H. Zhang, C. Qin, and Y. Luo, "Neural-Network-Based Constrained Optimal Control Scheme for Discrete-Time Switched Nonlinear System Using Dual Heuristic Programming", *IEEE Trans. Autom. Sci. Eng.* 11, 839–849 (2014).

[51] R. Kirlin, C. Lascu, and A. Trzynadlowski, "Shaping the Noise Spectrum in Power Electronic Converters", *IEEE Trans. Ind. Electron.* 58, 2780–2788 (2011).

[52] M. Auer and T. Karaca, "Spread spectrum techniques for Class-D audio amplifiers to reduce EMI", *e & i Elektrotechnik und Informationstechnik* 133, 43–47 (2016).

[53] MITSUBISHI ELECTRIC Semiconductors & Devices: Power Modules for Power Applications | Power supply / UPS. [Online]. https://www.mitsubishielectric.com/semiconductors/application/ups/index.html (accessed Aug. 11 2020).

[54] Silicon Carbide CoolSiC™ MOSFET Modules – Infineon Technologies. [Online] https://www.infineon.com/cms/en/product/power/mosfet/silicon-carbide/modules/ (accessed Aug. 11 2020).